

## Nonhydrolytic Synthesis of High-Quality Anisotropically Shaped Brookite TiO<sub>2</sub> Nanocrystals

Raffaella Buonsanti,<sup>†,‡</sup> Vincenzo Grillo,<sup>§</sup> Elvio Carlino,<sup>§</sup> Cinzia Giannini,<sup>||</sup>  
Tobias Kipp,<sup>⊥</sup> Roberto Cingolani,<sup>†,‡</sup> and Pantaleo Davide Cozzoli<sup>\*,†,‡</sup>

*Scuola Superiore ISUFI, University of Salento, Distretto Tecnologico, via per Arnesano km 5, 73100 Lecce, Italy, National Nanotechnology Laboratory of CNR-INFM, Unità di Ricerca IIT, Distretto Tecnologico ISUFI, via per Arnesano km 5, 73100 Lecce, Italy, TASC-INFM-CNR National Laboratory, Area Science Park—Basovizza, Bld MM, SS 14, Km 163.5, 34012 Trieste, Italy, CNR-Istituto di Cristallografia (IC), via Amendola 122/O, I-70126, Bari, Italy, and Institute of Applied Physics, University of Hamburg, Jungiusstrasse 11, 20355 Hamburg, Germany*

Received May 13, 2008; E-mail: davide.cozzoli@unile.it

**Abstract:** A surfactant-assisted nonaqueous strategy, relying on high-temperature aminolysis of titanium carboxylate complexes, has been developed to access anisotropically shaped TiO<sub>2</sub> nanocrystals selectively trapped in the metastable brookite phase. Judicious temporal manipulation of precursor supply to the reaction mixture enables systematic tuning of the nanostructure geometric features over an exceptionally wide dimensional range (30–200 nm). Such degree of control is rationalized within the frame of a self-regulated phase-changing seed-catalyzed mechanism, in which homogeneous nucleation, on one side, and heterogeneous nucleation/growth processes, on the other side, are properly balanced while switching from the anatase to the brookite structures, respectively, in a continuous unidirectional crystal development regime. The time variation of the chemical potential for the monomer species in the solution, the size dependence of thermodynamic structural stability of the involved titania polymorphs, and the reduced activation barrier for brookite nucleation onto initially formed anatase seeds play decisive roles in the crystal-phase- and shape-tailored growth of titania nanostructures by the present approach.

### 1. Introduction

Among transition-metal oxide materials, nanostructured TiO<sub>2</sub> has emerged in the past decades as an exclusive platform on which an exceptionally wide range of appealing solid-state physical–chemical properties coexist with the potential for low-cost and environmentally benign processes and energy technologies.<sup>1,2</sup> Apart from its traditional use in the preparation of cosmetics and functional ceramics, nanoscale TiO<sub>2</sub> has propelled both fundamental studies and practical applications in fields as diverse as optoelectronics, photovoltaics, thermally activated catalysis, ambient detoxification, sensing, fuel cells, lithium batteries, and hydrogen storage/production, raising each of them to a high level of performance.<sup>1,2</sup> Presently, increasingly sophisticated material fabrication strategies as well as innovative concepts are being pursued to extend the potential of TiO<sub>2</sub>-based technologies far beyond. These include design of advanced photocatalytic systems relying on controlled spatial

organization and interfacing of selected titania polymorphs,<sup>3,4</sup> realization of light-responsive coatings with simultaneous antireflective, antibacterial, self-cleaning, and antifogging behavior,<sup>5</sup> selective “green” synthesis of industrially relevant organic compounds and of fuel molecules under mild conditions,<sup>6</sup> and nanoparticle bioconjugation for cell targeting and photo therapeutic actions.<sup>7</sup>

The key to boost future advances in all promising technological areas that benefit from nanosized TiO<sub>2</sub> resides in the ability to develop nanostructures fulfilling a number of requirements, such as defined crystal phases and degree of crystallinity, engineered dimensions and shapes, and suitable chemical functionalities at the surface. Indeed, these features not only

- (3) (a) Kawahara, T.; Konishi, Y.; Tada, H.; Tohge, N.; Nishii, J.; Ito, S. *Angew. Chem., Int. Ed.* **2002**, *41*, 2811–2813. (b) Zhang, J.; Xu, Q.; Feng, Z.; Li, M.; Li, C. *Angew. Chem., Int. Ed.* **2008**, *47*, 1766–1769.
- (4) (a) Aprile, C.; Corma, A.; Garcia, H. *Phys. Chem. Chem. Phys.* **2008**, *10*, 769–783. (b) Li, G.; Gray, K. A. *Chem. Phys.* **2007**, *339*, 173–187.
- (5) (a) Fujishima, A.; Zhang, X. *C. R. Chim.* **2006**, *9*, 750–760. (b) Thompson, T. L.; Yates, J. T. *Chem. Rev.* **2006**, *106*, 4428–4453.
- (6) (a) Palmisano, G.; Augugliaro, V.; Pagliaro, M.; Palmisano, L. *Chem. Commun.* **2007**, 3425–3437. (b) Yurdakal, S.; Palmisano, G.; Loddo, V.; Augugliaro, V.; Palmisano, L. *J. Am. Chem. Soc.* **2008**, *130*, 1568–1569.
- (7) (a) Paunesku, T.; Rajh, T.; Wiederrech, G.; Maser, J.; Vogt, S.; Stojicevic, N.; Protic, M.; Lai, B.; Oryhon, J.; Thurnauer, M.; Woloschak, G. *Nat. Mater.* **2003**, *2*, 343. (b) Paunesku, T.; Vogt, S.; Lai, B.; Maser, J.; Stojicevic, N.; Thurn, K. T.; Osipo, C.; Liu, H.; Legnini, D.; Wang, Z.; Lee, C.; Woloschak, G. E. *Nano Lett.* **2007**, *7*, 596–601.

<sup>†</sup> University of Salento.

<sup>‡</sup> National Nanotechnology Laboratory of CNR-INFM.

<sup>§</sup> TASC-INFM-CNR National Laboratory.

<sup>||</sup> CNR-Istituto di Cristallografia.

<sup>⊥</sup> University of Hamburg.

- (1) Rodríguez, J. A.; Fernández-García, M. *Synthesis Properties, and Applications of Oxide Nanomaterials*; John Wiley & Sons, Inc.: Hoboken, NJ, 2007.
- (2) (a) Chen, X.; Mao, S. S. *Chem. Rev.* **2007**, *107*, 2891–2959, and references therein. (b) Chen, X.; Mao, S. S. *J. Nanosci. Nanotechnol.* **2006**, *6*, 906–925.

impact on the ultimate physicochemical behavior of the oxide itself but also on its interactions with the environment.<sup>2</sup> As of today, the general difficulty to achieve simultaneous control over both structural and geometric parameters represents the major obstacle precluding comparative assessment of the huge library of available TiO<sub>2</sub> nanomaterials, as well as delaying progress of the concerned technologies.<sup>1–7</sup>

Wet-chemical approaches have been especially distinguished for their versatility in tailoring TiO<sub>2</sub> in variety of mesoporous nanostructures, thin films, size- and shape-controlled nanocrystals and nanotubes.<sup>1,2</sup> As a major limitation, the impressive body of both synthetic and applicative research activities that have been so far carried out has dealt with the tetragonal anatase and rutile phases, due to the relative ease with which these polymorphs can be attained.<sup>2</sup> While enrichment of such knowledge is far from being exhausted, recent experimental and theoretical investigations have surprisingly highlighted that TiO<sub>2</sub> in the orthorhombic brookite crystal structure can indeed exhibit superior electrochemical,<sup>8,9</sup> catalytic,<sup>10,11</sup> and photocatalytic<sup>12–16</sup> performances over those offered by its anatase/rutile counterparts. Despite these promising findings, an in-depth elucidation of the inherent properties of brookite as well as significant advances in their practical exploitation remain yet hindered by the unsatisfactory level of control with which this polymorph is accessible on the nanoscale by means of state-of-art fabrication approaches.<sup>8–10,12,13,17–24</sup> It can thus be expected that development of refined synthetic routes allowing brookite nanostructures to be tailored with an elevated degree of both phase purity and size-morphological selectivity could contribute

to expand the technological potential of titania-based nanomaterials to a considerable extent.

The phase-controlled synthesis of TiO<sub>2</sub> nanostructures is particularly challenging in liquid media, whereby transformation of molecular precursors is affected by a complex interplay of thermodynamic and kinetic factors.<sup>25–27</sup> First, because of the strong contribution of the surface energy to the overall free energy in a nanocrystal system, the relative order of thermodynamic stability of the possible titania polymorphs becomes size- and shape-dependent and, hence, extremely sensitive to the chemical potential of reactive monomers as well as to the presence of surface-adhering species in the solution.<sup>2,28–33</sup> In addition, particle formation generally occurs far from equilibrium under kinetically driven growth regimes, in which processes such as reactant diffusion, facet-preferential adhesion of ligands, oriented attachment pathways, and ripening can be, in fact, more influential.<sup>2,25–27,30–33</sup> Owing to the relatively narrow energy stability window for brookite, reaction conditions that can guarantee both selective nanocrystal nucleation and growth in this crystal phase are inherently more restrictive than those required for obtaining either anatase or rutile. As a matter of fact, conventional aqueous precipitation or hydrothermal approaches frequently yield brookite as a minor contamination byproduct, while a number of experimental variables (e.g., water to precursor ratio, pH, catalysts, ionic strength, nature and concentration of chelating agents, temperature) need to be delicately adjusted in order to increase phase selectivity, however, at the cost of reproducibility.<sup>2,8–10,12,13,17–19,21–24,34,35</sup>

Powerful alternative pathways to general synthesis of nanoscale oxides are represented by nonaqueous sol–gel routes, which exploit organic molecules as both oxygen sources and capping agents under strict exclusion of water.<sup>26,27</sup> The overall preparation procedure is simplified, as the relative metal precursor to organic solvent/ligand concentration ratio and temperature are the only synthesis parameters that have to be regulated. Recently, nonhydrolytic schemes have been effectively applied to prepare shape-tailored TiO<sub>2</sub> nanocrystals in the anatase structure,<sup>2,26,27,36</sup> whereas access to either rutile or brookite has achieved scarce success, remaining in fact limited to nanostructures in specific dimensional–morphological regimes.<sup>8,20,36e</sup>

- (8) (a) Koelsch, M.; Cassaignon, S.; Guillemoles, J. F.; Jolivet, J. P. *Thin Solid Films* **2002**, *403*, 312–319. (b) Koelsch, M.; Cassaignon, S.; Minh, C. T. T.; Guillemoles, J. F.; Jolivet, J. P. *Thin Solid Films* **2004**, *451*, 86–92.
- (9) Lee, D.-H.; Park, J.-G.; Choi, K. J.; Choi, H.-J.; Kim, D.-W. *Eur. J. Inorg. Chem.* **2008**, 878–882.
- (10) Yan, W. F.; Chen, B.; Mahurin, S. M.; Dai, S.; Overbury, S. H. *Chem. Commun.* **2004**, *17*, 1918–1919.
- (11) Yan, W. F.; Chen, B.; Mahurin, S. M.; Schwartz, V.; Mullins, D. R.; Lupini, A. R.; Pennycook, S. J.; Dai, S.; Overbury, S. H. *J. Phys. Chem. B* **2005**, *109*, 10676–10685.
- (12) Shibata, T.; Irie, H.; Ohmori, M.; Nakajima, A.; Watanabe, T.; Hashimoto, K. *Phys. Chem. Chem. Phys.* **2004**, *6*, 1359–1362.
- (13) Addamo, M.; Bellardita, M.; Di Paola, A.; Palmisano, L. *Chem. Commun.* **2006**, *47*, 4943–4945.
- (14) Iskandar, F.; Nandiyanto, A. B. D.; Yun, K. M.; Hogan, C. J.; Okuyama, K.; Biswas, P. *Adv. Mater.* **2007**, *19*, 1408–1412.
- (15) Di Paola, A.; Addamo, M.; Bellardita, M.; Cazzanelli, E.; Palmisano, L. *Thin Solid Films* **2007**, *515*, 3527–3529.
- (16) Li, W.-K.; Gong, X.-Q.; Lu, G.; Selloni, A. *J. Phys. Chem. C* **2008**, *112*, 6594–6596.
- (17) Kominami, H.; Kohno, M.; Kera, Y. *J. Mater. Chem.* **2000**, *10*, 1151–1156.
- (18) Li, J. G.; Tang, C. C.; Li, D.; Haneda, H.; Ishigaki, T. *J. Am. Ceram. Soc.* **2004**, *87*, 1358–1361.
- (19) Tomita, K.; Petrykin, V.; Kobayashi, M.; Shiro, M.; Yoshimura, M.; Kakihana, M. *Angew. Chem., Int. Ed.* **2006**, *45*, 2378–2381.
- (20) (a) Tang, J.; Redl, F.; Zhu, Y. M.; Siegrist, T.; Brus, L. E.; Steigerwald, M. L. *Nano Lett.* **2005**, *5*, 543–548. (b) Trentler, T. J.; Denler, T. E.; Bertone, J. F.; Agrawal, A.; Colvin, V. L. *J. Am. Chem. Soc.* **1999**, *121*, 1613–1614.
- (21) Li, J. G.; Ishigaki, T.; Sun, X. D. *J. Phys. Chem. C* **2007**, *111*, 4969–4976.
- (22) (a) Cassaignon, S.; Koelsch, M.; Jolivet, J. P. *J. Mater. Sci.* **2007**, *42*, 6689–6695. (b) Cassaignon, S.; Koelsch, M.; Jolivet, J. P. *J. Phys. Chem. Solids* **2007**, *68*, 695–700.
- (23) Reyes-Coronado, D.; Rodríguez-Gattorno, G.; Espinosa-Pesqueira, M. E.; Cab, C.; de Coss, R.; Oskam, G. *Nanotechnology* **2008**, *19*, 145605.
- (24) Kobayashi, M.; Tomita, K.; Petrykin, V.; Yoshimura, M.; Kakihana, M. *J. Mater. Sci.* **2008**, *43*, 2158–2162.
- (25) (a) Cozzoli, P. D.; Pellegrino, T.; Manna, L. *Chem. Soc. Rev.* **2006**, *35*, 1195–1208. (b) Casavola, M.; Buonsanti, R.; Caputo, G.; Cozzoli, P. D. *Eur. J. Inorg. Chem.* **2008**, 837–854.
- (26) Cheon, Y.-w.; Choi, J.-s.; Cheon, J. *Angew. Chem., Int. Ed.* **2006**, *45*, 3414–3439.
- (27) (a) Niederberger, M. *Acc. Chem. Res.* **2007**, *40*, 793–800. (b) Niederberger, M.; Garnweitner, G.; Ba, J. H.; Polleux, J.; Pinna, N. *Int. J. Nanotechnol.* **2007**, *4*, 263–281.
- (28) Zhang, H.; Gilbert, B.; Huang, F.; Banfield, J. F. *Nature* **2003**, *424*, 1025–1029.
- (29) (a) Zhang, H.; Banfield, J. F. *J. Phys. Chem. B* **2000**, *104*, 3481–3487. (b) Ranade, M. R.; Navrotsky, A.; Zhang, H. Z.; Banfield, J. F.; Elder, S. H.; Zaban, A.; Borse, P. H.; Kulkarni, S. K.; Doran, G. S.; Whitfield, H. J. *Proc. Natl. Acad. Sci. U.S.A.* **2002**, *99*, 6476–6481. (c) Levchenko, A. A.; Li, G.; Boerio-Goates, J.; Woodfield, B. F.; Navrotsky, A. *Chem. Mater.* **2006**, *18*, 6324–6332.
- (30) Barnard, A. S.; Zapol, P. *J. Phys. Chem. B* **2004**, *108*, 18435–18440.
- (31) Barnard, A. S.; Curtiss, L. A. *Nano Lett.* **2005**, *5*, 1261–1266.
- (32) Barnard, A. S.; Zapol, P. *Phys. Rev. B* **2004**, *70*, 235403.
- (33) Barnard, A. S.; Zapol, P.; Curtiss, L. A. *J. Chem. Theory Comput.* **2005**, *1*, 107–116.
- (34) Zheng, Y. Q.; Shi, E. W.; Cui, S. X.; Li, W. J.; Hu, X. F. *J. Am. Ceram. Soc.* **2000**, *83*, 2634–2636.
- (35) (a) Bhave, R. C.; Lee, B. I. *Mater. Sci. Eng., A* **2007**, *467*, 146–149. (b) Lee, B. I.; Wang, X.; Bhave, R.; Hu, M. *Mater. Lett.* **2006**, *60*, 1179–1183. (c) Lee, J. H.; Yang, Y. S. *J. Mater. Sci.* **2005**, *40*, 2843–2847. (d) Lee, J. H.; Yang, Y. S. *J. Mater. Sci.* **2006**, *41*, 557–559.

Herein, we report, for the first time, a straightforward surfactant-assisted nonaqueous strategy by which high-quality anisotropically shaped TiO<sub>2</sub> nanocrystals can be synthesized in the exclusive brookite crystal structure with geometric features tunable over an exceptionally wide dimensional range (30–200 nm). Our method relies on suitable temporal manipulation of the aminolysis reaction of titanium oleate complexes, which takes place during the high-temperature treatment of mixtures of titanium tetrachloride, oleic acid, and oleyl amine under water- and oxygen-free conditions. Simultaneous size-morphological and crystal-phase tailoring of TiO<sub>2</sub> nanostructures is demonstrated by means of a precursor supply technique that combines a slow-heating step with subsequent delivery of additional reactants at a controllably low rate. Our results are explained within the frame of a self-regulated phase-changing seed-catalyzed mechanism, in which homogeneous nucleation, on one side, and heterogeneous nucleation and growth processes, on the other side, are properly balanced while switching from the anatase to the brookite structures, respectively, in a continuous unidirectional crystal development regime. The time variation of the chemical potential for the monomers in the solution, the size dependence of thermodynamic structural stability of the involved TiO<sub>2</sub> polymorphs, and the reduced activation barrier for brookite nucleation onto initially formed anatase seeds are considered to play key roles in the phase-controlled growth of the nanostructures by the present approach.

## 2. Experimental Section

**2.1. Synthesis Procedures.** **2.1.1. Materials.** All chemicals were of the highest purity available and were used as received; titanium(IV) chloride (TiCl<sub>4</sub>, 99.999%), titanium(IV) isopropoxide (Ti(O<sup>i</sup>Pr)<sub>4</sub> or TTIP, 99.999%), oleic acid (C<sub>17</sub>H<sub>33</sub>CO<sub>2</sub>H or OLAC, 90%), oleyl amine (C<sub>17</sub>H<sub>33</sub>NH<sub>2</sub> or OLAM, 70%), trimethylamine *N*-oxide dihydrate ((CH<sub>3</sub>)<sub>3</sub>NO·2H<sub>2</sub>O or TMAO, 98%), and 1-oc-tadecene (C<sub>18</sub>H<sub>36</sub> or ODE, 90%) were purchased from Aldrich. All solvents used were of analytical grade and purchased from Aldrich. Water was bidistilled (Millipore Q).

**2.1.2. Standard Synthesis of TiO<sub>2</sub> Nanorods.** Unless otherwise stated, all syntheses were carried out under air-free conditions using a standard Schlenk line setup. As a general procedure to TiO<sub>2</sub> nanorods, 3 g of ODE, 13–52 mmol of OLAM, and 0.5–2 mmol of OLAC were loaded into a three-neck flask and degassed at 120 °C for 30 min, after which the mixture was cooled down to 50 °C under N<sub>2</sub> flow. At this point, 0.5–2 mmol of TiCl<sub>4</sub> was added (such that the OLAC/TiCl<sub>4</sub> molar ratio was 1), and the flask was heated up to 290 °C at a ramp rate of ~25 °C/min. As the temperature was increased, the solution turned from colorless to pale yellow, to dark brown, and finally to white milky. After heating for 30 min at 290 °C, the reaction could be either halted, by removing the heating mantle and allowing rapid cooling, or continued upon addition of a room-temperature feedstock precursor solution of an equimolar TiCl<sub>4</sub>/OLAC mixture in ODE (prepared in a separated flask under N<sub>2</sub>) at a constant rate of 0.1 mL/min by means of a syringe pump (GENIE Plus Syringe Pump, Kent Scientific). The largest nanorods were obtained by injecting up to an additional 20 mmol of TiCl<sub>4</sub> to the initial mixture.

**2.1.3. Extraction Procedures.** After the synthesis, the extraction/purification procedures of the nanocrystals were carried out under ambient atmosphere. The TiO<sub>2</sub> product was separated from its growing mixture upon acetone (or 2-propanol) addition and subsequent centrifugation (5000 rpm), after which it was thoroughly washed with acetone to remove precursor and surfactant/ODE residuals. The purified nanocrystals were finally dispersed into nonpolar solvents, such as chloroform, toluene, or hexane, providing stable either optically clear colloidal solutions or suspensions, depending on the average size of the nanorods (see Figure S7 in

the Supporting Information). If necessary, minor sample contamination by much smaller (<8–10 nm) and irregularly shaped nanoparticles could be easily eliminated by performing a single size-selective precipitation step upon combining calibrated 2-propanol addition with low-speed centrifugation (2000–3000 rpm), after which the supernatant was discarded.

**2.1.4. Monitoring Nanocrystal Growth.** The temporal evolution of reaction byproducts as well as of nanocrystal growth was monitored by performing transmission electron microscopy (TEM), X-ray diffraction (XRD), Raman, and Fourier transform infrared spectroscopy (FT-IR) analyses on aliquots of the hot surfactant mixture extracted via a glass syringe at scheduled time intervals. The aliquots were suddenly cooled down and eventually subjected to TiO<sub>2</sub> extraction procedures described above.

**2.1.5. Control Seeded-Growth Experiments.** As control growth experiments, the synthesis of nanorods with increasingly higher aspect ratios was attempted by applying a seeded-growth technique.<sup>25</sup> To this aim, phase-controlled nanorods were first prepared in an independent synthesis step, then thoroughly purified, and finally employed as the starting seeds for producing comparatively larger nanorods in fresh TiCl<sub>4</sub>/OLAC/OLAM mixtures, using the standard protocol described earlier. Nanorod seeds in the brookite structure (with minimum dimensions of ~3–4 nm × 30 nm) were synthesized by the slow heating of TiCl<sub>4</sub>/OLAC/OLAM mixtures, as illustrated above. The *c*-axis-elongated TiO<sub>2</sub> nanorod seeds in the pure anatase phase were obtained by two literature methods, namely, the high-temperature TTIP decomposition in OLAC/OLAM mixtures<sup>36a</sup> and TMAO-catalyzed hydrolysis of TTIP at 100 °C.<sup>37</sup>

**2.2. Characterization Techniques.** **2.2.1. Raman Spectroscopy.** Measurements were performed on dried TiO<sub>2</sub> nanocrystal films deposited onto an indium tin oxide (ITO) substrate from the corresponding colloidal solutions. Raman experiments were performed at room temperature by using a diode-pumped solid-state laser ( $\lambda = 532$  nm, 15 mW) that was coupled into an optical microscope with a 100× objective lens, which focused a 1  $\mu$ m light spot onto the sample surface. The Raman scattered light was collected by the same objective and spectrally analyzed by a triple Raman spectrometer (Dilor XY, with a resolution of about 1 cm<sup>-1</sup>) equipped with a Peltier-cooled, deep-depletion CCD detector. Typical acquisition times were on the order of 200 s, during which about 80 spectra were recorded and averaged.

**2.2.2. Fourier Transform Infrared Spectroscopy.** Infrared spectroscopy measurements in the 4000–400 cm<sup>-1</sup> spectral range were carried out on samples deposited on silicon substrates using a Bruker Equinox 70 FT-IR apparatus in transmission mode at a resolution of 4 cm<sup>-1</sup>.

**2.2.3. X-ray Diffraction.** Powder XRD measurements were performed with a Bruker D8 Discover diffractometer equipped with a 3 kW ceramic tube with a copper anode, a Goebel-type parabolic mirror, and a NaI(Tl) scintillator detector. Concentrated solutions of the purified nanocrystals were spread on top of a silicon substrate. The sample was allowed to dry and then measured in reflection geometry.

A whole profile XRD fitting was performed by using FULL-PROF software which allows the shape anisotropy of the nanocrystalline sample to be described by means of spherical harmonics.<sup>38</sup> The accuracy of the fitting evaluation was estimated by a goodness-

(36) (a) Zhang, Z. H.; Zhong, X. H.; Liu, S. H.; Li, D. F.; Han, M. Y. *Angew. Chem., Int. Ed.* **2005**, *44*, 3466–3470. (b) Seo, J.-w.; Jun, Y.-w.; Ko, S. J.; Cheon, J. *J. Phys. Chem. B* **2005**, *109*, 5389–5391. (c) Jun, Y. W.; Casula, M. F.; Sim, J. H.; Kim, S. Y.; Cheon, J. *J. Am. Chem. Soc.* **2003**, *125*, 15981–15985. (d) Joo, J.; Kwon, S. G.; Yu, T.; Cho, M.; Lee, J.; Yoon, J.; Hyeon, T. *J. Phys. Chem. B* **2005**, *109*, 15297–15302. (e) Koo, B.; Park, J.; Kim, Y.; Choi, S.-H.; Sung, Y.-E.; Hyeon, T. *J. Phys. Chem. B* **2006**, *110*, 24318–24323.

(37) Cozzoli, P. D.; Kornowski, A.; Weller, H. *J. Am. Chem. Soc.* **2003**, *125*, 14539–14548.

(38) Crystallographic tools for Rietvel, profile matching and integrated intensity refinements of X-ray and/or neutron data, available online at <http://wwwold.ill.fr/dif/Soft/fp/php/downloads.html>.

of-fit statistical indicator (GoF), which takes the value of 1 for an ideal fit. GoF values of  $<3-4$  were considered satisfactory.

**2.2.4. Transmission Electron Microscopy.** Low-resolution TEM images were recorded with a Jeol Jem 1011 microscope operated at an accelerating voltage of 100 kV. Phase-contrast high-resolution transmission electron microscopy (HRTEM) experiments were performed by using a Jeol 2010F TEM/STEM microscope operated at 200 keV, which corresponded to an electron wavelength of 0.00251 nm. The objective lens had a spherical aberration coefficient of  $0.47 \pm 0.01$  nm and hence a resolution at optimum defocus of 0.19 nm in HRTEM<sup>39a</sup> and of 0.126 nm in annular dark-field imaging.<sup>39b</sup> Samples for analysis were prepared by dropping a dilute nanocrystal solution in toluene onto carbon-coated Cu grids and then allowing the solvent to evaporate.

The spatial distribution of the different TiO<sub>2</sub> polymorphs in the nanorods was obtained, as described elsewhere.<sup>40</sup> A crystal-phase map was derived by analyzing the local amplitude of the periodicity characteristic of each crystal phase. To obtain the amplitude as a point-to-point information, the Fourier transform of the image was considered according to the method of Hytch et al.<sup>41</sup> The contribution to the image, arising from each Fourier peak, can be written as

$$I(\vec{r}) \approx H_{\vec{g}}(\vec{r})e^{i2\pi\vec{g}\vec{r}} \quad (1)$$

where  $I(\vec{r})$  is the image intensity at the position vector  $\vec{r}$ ,  $\vec{g}$  is the reciprocal lattice vector, and the factor  $H_{\vec{g}}(\vec{r})$  represents the local value of the Fourier coefficient of the fringes. To extract  $H_{\vec{g}}(\vec{r})$ , the selected Fourier peak was isolated by multiplying it with a Gaussian mask,  $M(\vec{k})$ :<sup>41</sup>

$$M(\vec{k}) = e^{-\frac{(\vec{k} - \vec{g})^2}{\sigma^2}} \quad (2)$$

(where  $\sigma$  is the width of the mask and  $\vec{k}$  is the relevant image spatial frequency) in order to exclude other periodicities ( $\sigma$  was chosen of the order of  $5 \text{ nm}^{-1}$ ). The as-derived Fourier spectrum was then back-transformed, and the resulting image was multiplied by  $e^{i2\pi\vec{g}\vec{r}}$  in order to remove the exponential factor. The amplitude of  $H_{\vec{g}}(\vec{r})$  was then derived to construct a map of the local amplitude of the image interference. The maps obtained by this method were superimposed using a different color for each phase. The spatial resolution of this technique is determined by the size of the Gaussian mask that imposes a limited bandwidth to the resulting map.

### 3. Results and Discussion

The general procedure that has been developed to synthesize simultaneously crystal-phase- and shape-controlled TiO<sub>2</sub> nanocrystals consists of an initial decomposition of TiCl<sub>4</sub> in an OLAC/OLAM/ODE mixture at 290 °C under inert atmosphere, which is eventually followed by calibrated supply of additional TiCl<sub>4</sub>/OLAC feedstock precursors. This technique ensures nucleation and growth of titania to occur preferentially in either the anatase or the brookite structure, respectively, under all-unidirectional crystal development conditions. The level of size-morphological and crystal-phase control achievable by this strategy can be appreciated from the low-magnification TEM galleries in Figures 1 and 2 and from the detailed structural analyses presented in Figures 3–7 by means of powder XRD, Raman spectroscopy,

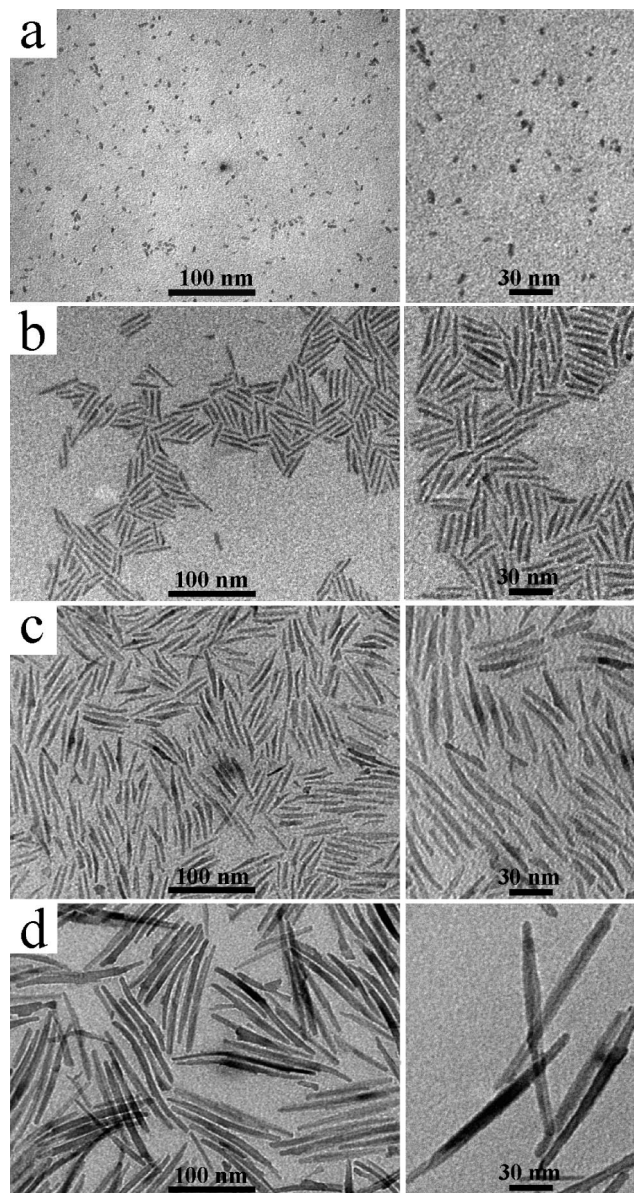


**Figure 1.** Low- and high-magnification (left and right panels, respectively) TEM overview of TiO<sub>2</sub> nanocrystals synthesized at lower OLAM/OLAC ratios. The flask, containing 0.5 mmol of TiCl<sub>4</sub>, 0.5 mmol of OLAC, 13 mmol of OLAM, and 3 g of ODE, was slowly heated up to 290 °C and kept at this temperature for 30 min (a). Subsequently, varying amounts of an equimolar TiCl<sub>4</sub>/OLAC mixture were added at a rate of 0.1 mL/min at 290 °C: (b) 2 mmol; (c) 8 mmol; (d) 20 mmol.

and HRTEM, respectively. As relevant cases of study, here we compare the results of two sets of syntheses carried out in the presence of fixed absolute amounts of ODE (3 g) and OLAM (13 or 52 mmol) in the flask.

Single-step syntheses based on the slow heating of less than 1 mmol of TiCl<sub>4</sub> in the presence of the selected surfactant media yield nearly isotropic  $\sim 3$  nm nanocrystals at lower OLAM concentration (Figure 1a), while tiny nanorods with a diameter of  $\sim 3$  nm and length of  $\sim 15-20$  nm are already formed at significantly higher amine content (Figure 2a). Upon loading the initial reaction medium with further TiCl<sub>4</sub> up to 2 mmol, and subsequently feeding the system with gradually larger volumes of TiCl<sub>4</sub>/OLAC stock precursor solution at a controllably slow rate at 290 °C, a continuous anisotropic nanocrystal growth regime is established. Monodisperse rod-shaped TiO<sub>2</sub>

(39) (a) Spence, J. *Experimental High-Resolution Electron Microscopy*; Oxford University Press: New York, 1988; p 87. (b) Carlino, E.; Grillo, V. *Proceedings of the 7th Multinational Congress on Microscopy—MCM 2005*, Portoroz, Slovenia, June 26–30, 2005; Slovene Society for Microscopy and Department of Nanostructured Materials, Jozef Stefan Institute: Ljubljana, Slovenia, 2005; p 6303.

(40) Buonsanti, R.; Grillo, V.; Carlino, E.; Giannini, C.; Curri, M. L.; Innocenti, C.; Sangregorio, C.; Achterhold, K.; Parak, F. G.; Agostiano, A.; Cozzoli, P. D. *J. Am. Chem. Soc.* **2006**, *128*, 16953–16970.

(41) Hytch, M. J.; Snoeck, E.; Kilaas, R. *Ultramicroscopy* **1998**, *74*, 131.

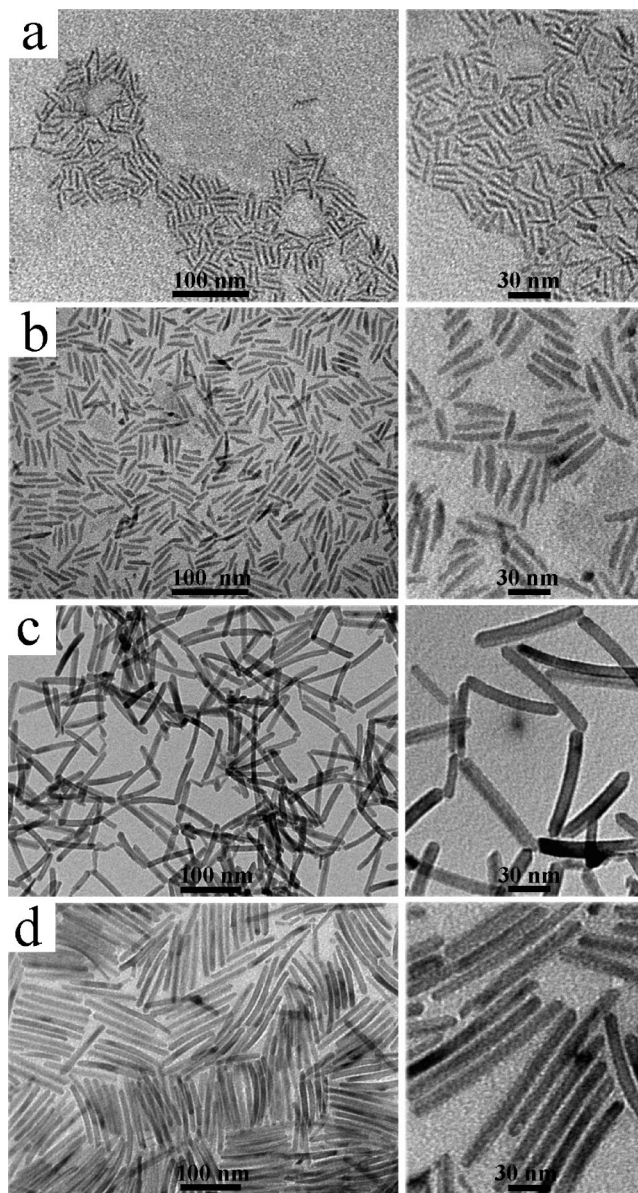


**Figure 2.** Low- and high-magnification (left and right panels, respectively) TEM overview of TiO<sub>2</sub> nanocrystals synthesized at higher OLAM/OLAC ratios. The flask, containing 0.5 mmol of TiCl<sub>4</sub>, 0.5 mmol of OLAC, 52 mmol of OLAM, and 3 g of ODE, was slowly heated up to 290 °C and kept at this temperature for 30 min (a). Subsequently, varying amounts of an equimolar TiCl<sub>4</sub>/OLAM mixture in ODE were added at a rate of 0.1 mL/min at 290 °C: (b) 2 mmol; (c) 12 mmol; (d) 20 mmol.

nanostructures, for which expansion along the longitudinal axis direction is progressively accentuated over the enlargement of the transverse axis, are indeed found as the exclusive product (Figure 1b–d and Figure 2b–d). TEM clarifies that unidirectional particle development proceeds via successive incorporation of monomers into the either spherical or rodlike small titania nanocrystals, henceforth referred to as the “seeds”, which are initially generated during the slow-heating step. The involvement of oriented attachment growth pathways is in fact discredited by the observation that the relative percentage of elongated nanocrystals within the particle population remains high and almost constant over the entire synthesis course. By adjusting the experimental conditions, a continuous tailoring of the diameter and the length sizes is achieved in the 3–10 and 30–200 nm intervals, respectively, which ultimately transcribes

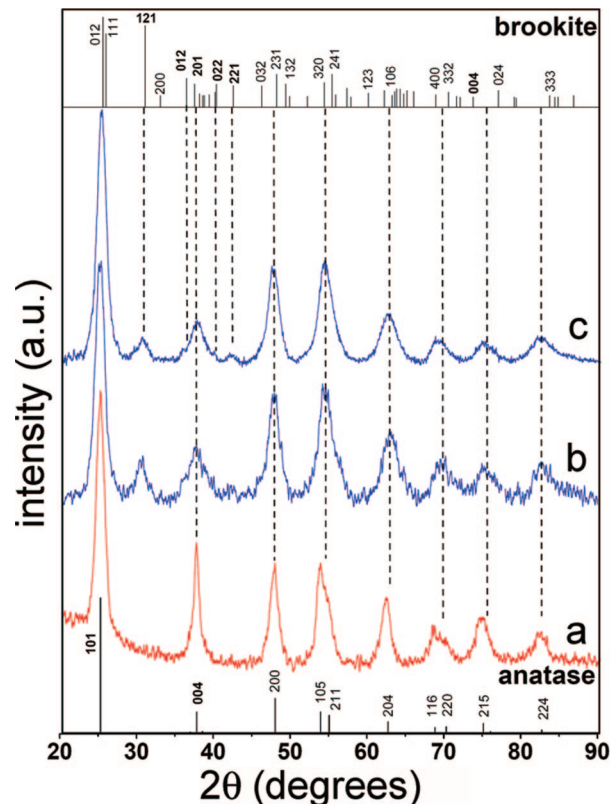


**Figure 3.** Powder XRD patterns of TiO<sub>2</sub> nanorods with different dimensions: (a) 3 nm × 20 nm; (b) 4 nm × 50 nm; (c) 8 nm × 200 nm. The reference diffraction patterns of bulk brookite and anatase are reported in the top and bottom part of the figure, respectively.

into nanorods with aspect ratio spanning from ~3 to ~20. The comparative TEM overviews also suggest that the surfactant composition impacts on the synthesis outcome. On one hand, the presence of OLAM in reduced proportions relative to OLAC promotes tapering of the nanorod terminations into arrow-shaped tips and attributes a pronounced curvature to the nanostructures with higher aspect ratios (Figure 1b–d). On the other side, higher OLAM/OLAC ratios contribute to anticipate the onset of anisotropic growth (cf., Figure 1a and Figure 2a) and assist formation of regular nanocrystals with a rectangular-shaped profile, which exhibit slight longitudinal bending (Figure 2b–d).

Overall, the results just presented above represent a remarkable leap forward in the engineering of low-dimensional titania nanostructures. Indeed, the ability of regulating the geometric features of TiO<sub>2</sub> nanorods in a gradual and systematic way over a broad dimensional range by means of a unique chemical synthesis route has been rarely documented in the literature.<sup>2,36e</sup>

Powder XRD and Raman spectroscopy analyses reveal the occurrence of a structural transition at a critical titania nanocrystal size threshold. The XRD profile of the spherical and low aspect ratio anisotropic particles with dimensions below ~20 nm (similar to those in Figure 1a–b and Figure 2a, respectively) is fully consistent with the formation of nanosized domains in the tetragonal anatase TiO<sub>2</sub> polymorph. In particular, the pattern of the nanorods differs from that of the bulk reference by the more pronounced and sharper {004} peak, as well as by minor alterations in the relative intensities and widths of other reflections, which authenticates a preferential lattice elongation in the *c*-axis direction (Figure 3, part a).<sup>2,36,37</sup> Accordingly, the corresponding Raman spectra exhibit the typical longitudinal optical modes of anatase, namely, two E<sub>g</sub> peaks (151, 644 cm<sup>-1</sup>),

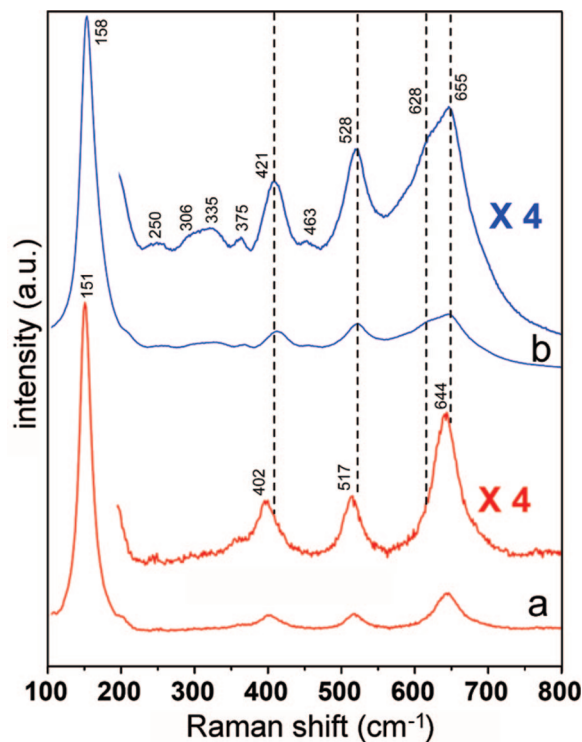


**Figure 4.** Representative Raman spectra of TiO<sub>2</sub> nanorods with different dimensions: (a) 3 nm × 20 nm; (b) 8 nm × 200 nm.

one B<sub>1g</sub> peak (402 cm<sup>-1</sup>), and unresolved A<sub>1g</sub>/B<sub>1g</sub> peaks (517 cm<sup>-1</sup>), respectively (Figure 4, part a).<sup>42a,b</sup> As a consequence of phonon confinement, these signals are blue-shifted and exhibit larger and asymmetrically broadened line widths, as compared to those observed for the bulk material.<sup>2</sup> In contrast to these findings, the structural identity of the nanorods with longer mean lengths (above 25–30 nm) and aspect ratios (as those shown in Figure 1c–d, and Figure 2b–d) diverges remarkably from that of the smaller precursor seeds from which they are derived. On one hand, the corresponding XRD patterns (Figure 3, parts b and c) disclose several peculiarities that support the formation of the orthorhombic brookite polymorph and its dominance in nanorods in this upper size regime: first, the suppression of the characteristic {004} peak inherent to the pristine anisotropic anatase domains; second, the appearance and intensification of the distinctive {121}, {012}, {022}, and {221} reflections; finally, a broadening and shift of the major peaks at higher angles, at which a close matching is established with numerous reflections of the brookite reference. Alterations in the relative intensity ratios of various reflections, compared to those found in the bulk diffraction pattern of brookite, can be interpreted as a signature of unidirectional crystal development, although the preferential lattice elongation in the *c*-axis direction, which will be demonstrated by HRTEM in the next paragraphs, cannot be unambiguously appreciated due to the convolution of the low-scattering {004} reflection with a number of signals in the same 2θ region. A satisfactory fitting of the XRD experimental data has been accomplished by means of an appropriate software program accounting for nanocrystal shape anisotropy (Figures S1–S2 in the Supporting Information), which therefore confirms the attributions made above. In agreement with the XRD results, the corresponding Raman spectra show a rich scenario of signals (Figure 4, part b), as commonly encountered for both natural and artificial brookite.<sup>12,17–19,21–24,34,35,42c</sup> Characteristic bands

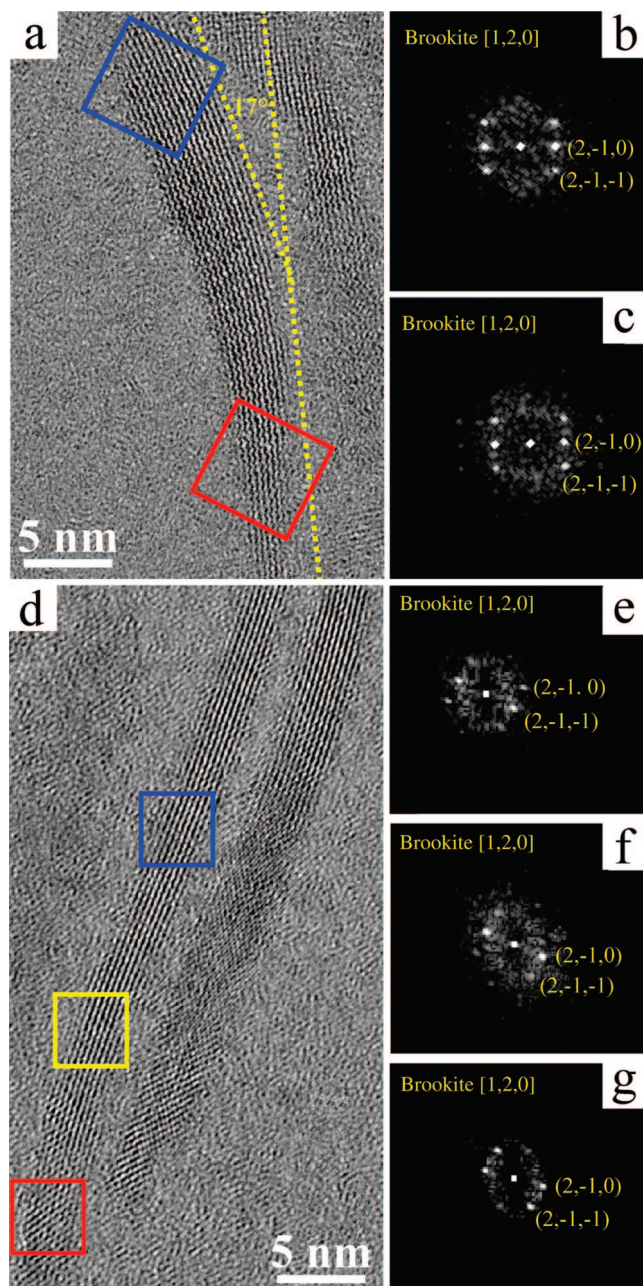


**Figure 5.** (a and d) HRTEM images of individual [0,0,1]-elongated brookite TiO<sub>2</sub> nanorods with aspect ratio of about 6, viewed along the (1,2,0) zone axis. (b and c) Diffraction patterns obtained from the regions enclosed by the blue and red boxes in panel a, respectively. (e–g) Diffraction patterns obtained from the regions enclosed within the blue, yellow, and red boxes in panel d, respectively.

include the most intense A<sub>1g</sub> mode (158 cm<sup>-1</sup>) and the much weaker A<sub>1g</sub> or B<sub>2g</sub> (250 cm<sup>-1</sup>), B<sub>2g</sub> (335, 375 cm<sup>-1</sup>), and B<sub>3g</sub> or B<sub>3g</sub> (306 cm<sup>-1</sup>) vibrations. Other major features are tentatively assigned as B<sub>1g</sub> or A<sub>1g</sub> (421 cm<sup>-1</sup>), B<sub>1g</sub> or B<sub>3g</sub> (463, 528 cm<sup>-1</sup>), A<sub>1g</sub> and/or B<sub>3g</sub> modes (628, 655 cm<sup>-1</sup>), which are in fact exceedingly prominent and shifted in wavenumber to be otherwise attributed to residual anatase.<sup>42</sup> Unfortunately, any direct comparison of our spectral data with literature studies remains elusive at this stage, since the Raman scattering efficiency as well as the relative band intensities are expected to be complicatedly dependent on many sample features apart from the crystal phase, such as local lattice imperfections, nanocrystal

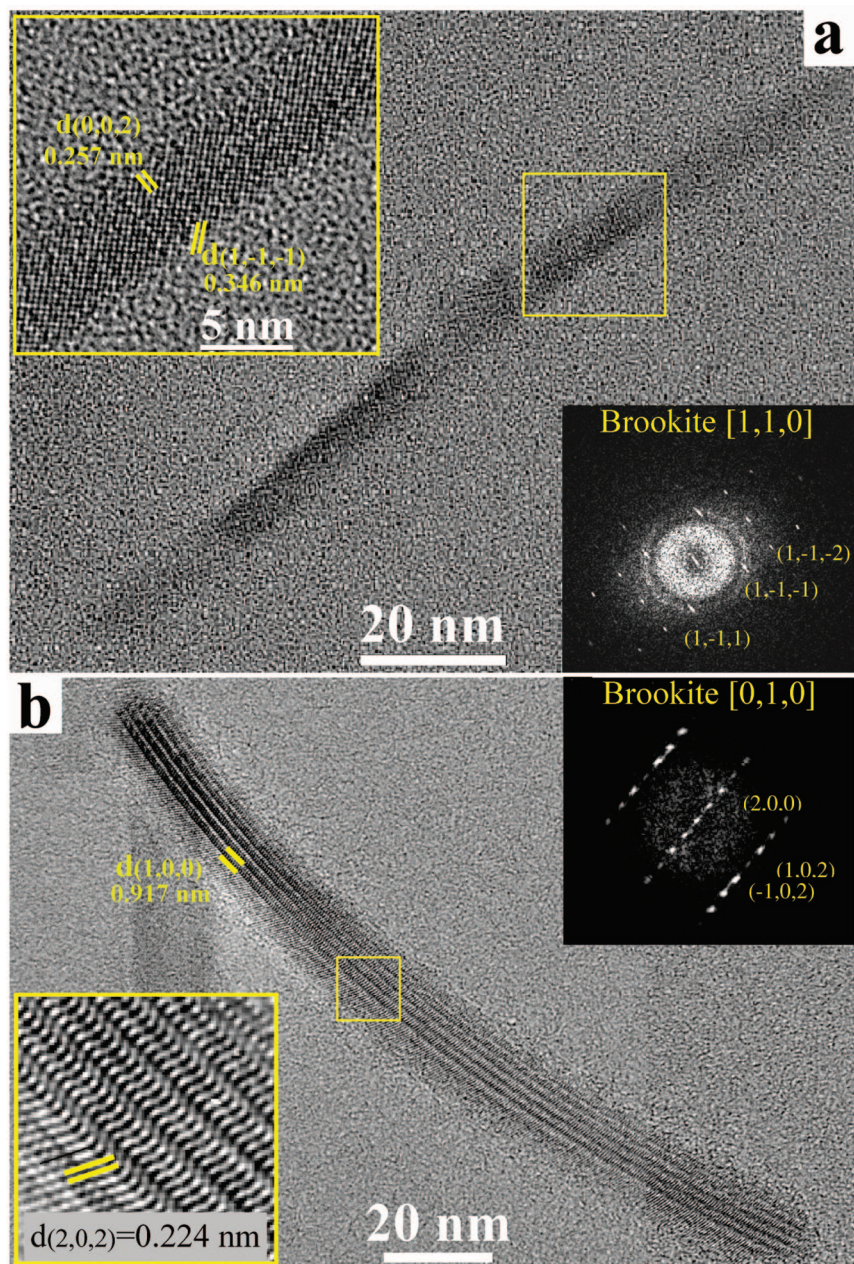


**Figure 6.** Representative HRTEM images of individual brookite [0,0,1]-elongated TiO<sub>2</sub> nanorods with aspect ratio of about 18. The panels show curved nanostructures with a tapered (a) and banana-like morphology (b) viewed along their  $\langle 1,1,0 \rangle$  and  $\langle 0,1,0 \rangle$  zone axes, respectively. The corresponding insets display the relevant diffractograms and identification of characteristic lattice spacings of brookite.

size and shape, surface status, and defect density, which have yet to be elucidated for brookite.<sup>8–10,12,17–19,21–24,34,35</sup>

Phase-contrast HRTEM investigations, along with the fast Fourier transform (FFT) of the relevant images, provide detailed information on the structure of the nanorods, enabling, in most cases, unambiguous discrimination between the possible TiO<sub>2</sub> polymorphs for nanocrystals suitably aligned with respect to the electron beam. Our analyses demonstrate that, although the smaller nanorods indeed occur as *c*-axis-elongated anatase, which thus reiterates previous data,<sup>2,26,27,36,37</sup> the high-aspect ratio nanostructures in the 30–200 nm range are instead single-crystalline objects made of brookite TiO<sub>2</sub> with a preferential lattice extension in the *c*-axis direction. Figure 5 illustrates representative studies of such nanocrystals. The first case focuses on a bent nanorod along its  $\langle 1,2,0 \rangle$  zone axis (Figure 5a). It comprises two main straight sections at the opposite sides of a

central curved region, which are rotated by about 17° with respect to each other, as deduced by measuring the angle between the directions of the  $\{2,1,0\}$  longitudinal facets that enclose them. The FFT patterns corresponding to both nanorod segments are identical and univocally assignable as brookite (Figure 5b–c). In the second case of HRTEM study, the interpretation of the image is less obvious (Figure 5d). The diffractograms corresponding to three different regions of the nanorod under observation differ slightly from each other, which can be ascribed to subtle lattice deformation across the nanostructure. Indeed, while the first FFT pattern (Figure 5e) matches almost perfectly with brookite in its  $\langle 1,2,0 \rangle$  zone axis, the others diverge gradually (Figure 5f–g) and to such an extent that the last diffractogram could be even misinterpreted as anatase down the  $\langle 1,0,0 \rangle$  zone axis. Nevertheless, the hypothesis of a composite brookite–anatase nanorod is here discredited

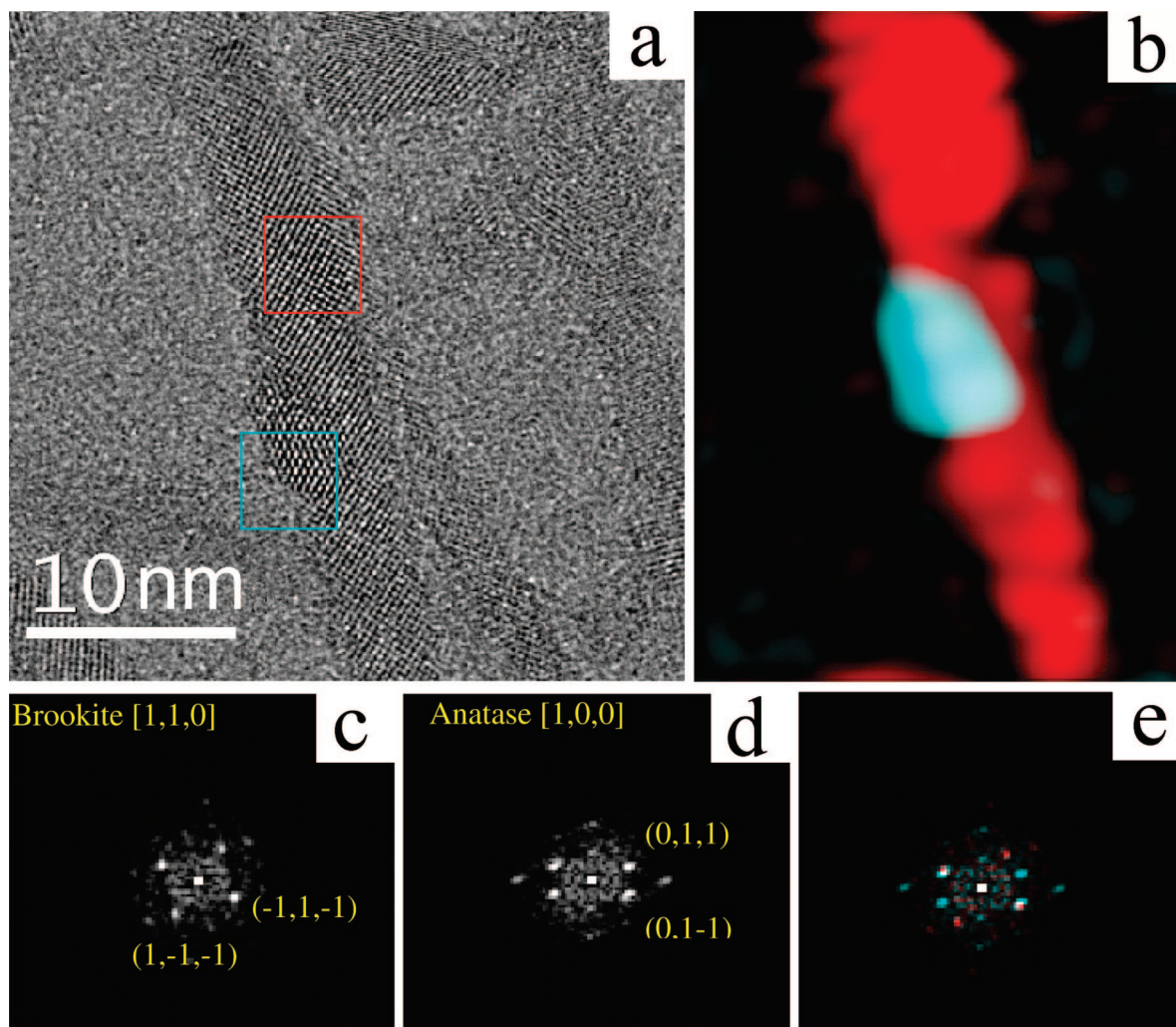


**Figure 7.** (a) Representative HRTEM image of a biphasic heterostructured  $\text{TiO}_2$  nanorod showing incomplete anatase-to-brookite conversion. (b) False-color crystal-phase map obtained by periodicity analysis of the image in panel a: the red color is related to the amplitude of the  $(1,-1,-1)$  fringes of brookite, whereas the blue color refers to the  $(0,1,1)$  fringes of anatase. (c and d) Diffraction patterns obtained from the region enclosed by the blue and the red boxes in panel a, respectively, which correspond to brookite viewed along the  $\langle 1,1,0 \rangle$  and anatase viewed along the  $\langle 1,0,0 \rangle$ . (e) Merging of the two diffraction patterns in panels c and d, each traced by a different color (note that the white spots in panel e are due to coincidence of lattice spacings of the two polymorphs).

by the fact that the transition across the diffraction patterns is not accompanied by the identification of any clear interface. Similar arguments equally apply to the structural elucidation of much larger nanorods with higher aspect ratios (Figure 6). The reported examples of curved nanostructures, one with a tapered profile viewed along the  $\langle 1,1,0 \rangle$  (Figure 6a) and the other one with a banana-like morphology viewed along the  $\langle 0,1,0 \rangle$  (Figure 6b), demonstrate retention of the brookite structure at such large sizes and the preferential lattice elongation in the  $c$ -axis direction. In particular, in Figure 6b, the joint effects of the large nanocrystal thickness and of the subtle (i.e., by  $0.3^\circ$ ) misalignment of the nanostructure relative to its exact  $\langle 0,1,0 \rangle$  zone axis contribute to enhance the visibility of the kinematically forbidden  $\{1,0,0\}$  periodicities, corresponding to a lattice spacing of  $d_{100} = 0.917$  nm. Such interpretation is actually corroborated by pertinent HRTEM simulations of the experimental image (Figure S3 in the Supporting Information). Additionally, under the observed projections, other families of facets are identifiable, such as the  $\{2,-2,0\}$ - and  $\{1,0,0\}$ -type surfaces (in Figure 6, parts a and b, respectively). The generally inferred dominance of the longitudinal  $\{210\}/\{100\}$  planes, and of the basal  $\{001\}$  facets in the nanorod surface arrangement, corresponds well to

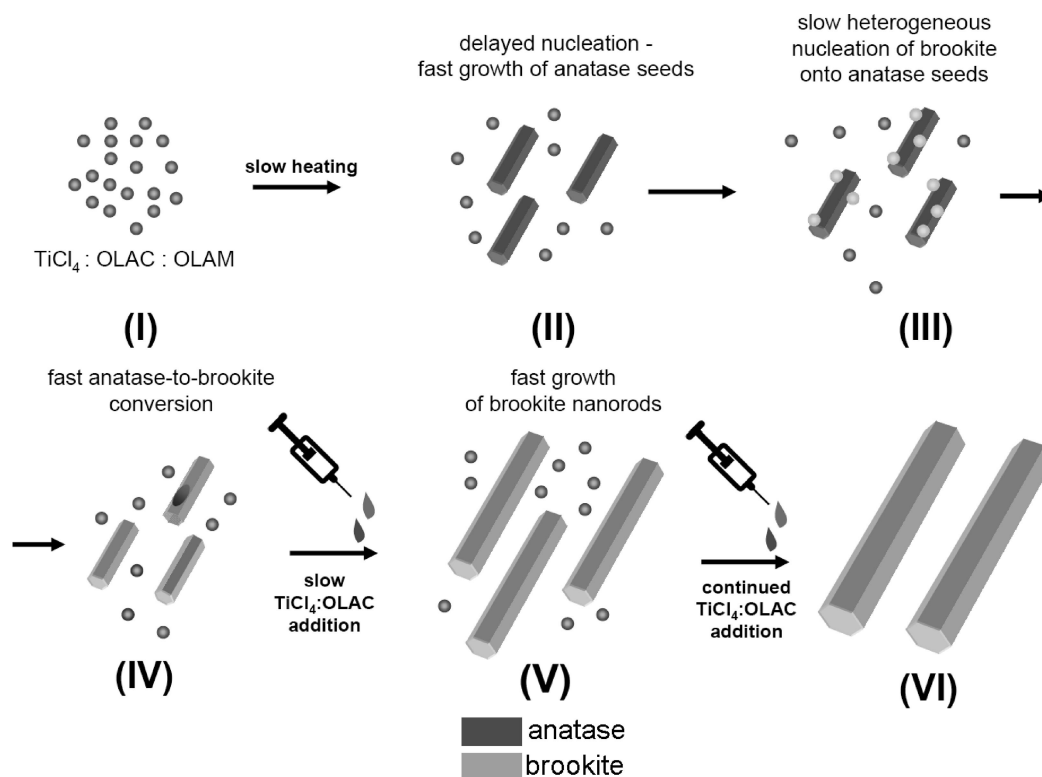
that expected for equilibrium shape brookite crystals, as derived by the Wulff construction.<sup>43</sup>

We have studied the formation pathways, through which the brookite nanorods are achieved, by carrying out pertinent series of control experiments as well as of chemical and structural–morphological analyses on the reaction mixture products at different reaction times. Our investigations suggest operation of a self-controlled phase-changing seed-catalyzed mechanism, sketched in Scheme 1, according to which homogeneous nucleation, on one side, and heterogeneous nucleation and growth processes, on the other side, can switch from the anatase to the brookite structures, respectively, in an appropriately balanced manner. These conclusions are supported by the following arguments.

The prolonged heating of  $\text{TiCl}_4$  with either OLAM or OLAC alone does not yield any detectable oxide precipitate, although

(42) (a) Zhang, W. F.; He, Y. L.; Zhang, M. S.; Yin, Z.; Chen, Q. *J. Phys. D: Appl. Phys.* **2000**, *33*, 912–916. (b) Scepanovic, M. J.; Grujic-Brojcin, M. U.; Dohcevic-Mitrovic, Z. D.; Popovic, Z. V. *Mater. Sci. Forum* **2006**, *518*, 101–106. (c) Tompsett, G. A.; Bowmaker, G. A.; Cooney, R. P.; Metson, J. B.; Rodgers, K. A.; Seakins, J. M. *J. Raman Spectrosc.* **1995**, *26*, 57–62.

(43) Gong, X. Q.; Selloni, A. *Phys. Rev. B* **2007**, *76*, 235307.

**Scheme 1.** Proposed Seed-Catalyzed Phase-Changing Mechanism for the Formation of Brookite Nanorods

sequences of color and vibrational spectra changes point to the generation and interconversion of various types of mono- or polynuclear titanium amino chloride or oleate complexes, in the respective cases (Figures S4–S5 in the Supporting Information). Conversely, in OLAM/OLAC/TiCl<sub>4</sub> mixtures (Figure S6 in the Supporting Information), OLAM not only catalyzes formation of titanium carboxylates, but also triggers their aminolysis, thereby producing TiO<sub>2</sub> with oleyl amide as the elimination byproduct.<sup>36a</sup> This is consistent with the fact that the final nanorods ultimately retain mainly an OLAM capping at their surface (Figure S7 in the Supporting Information).

The key to realizing the high level of size and morphological control of the TiO<sub>2</sub> nanostructures reported here relies on regulating the temporal variation of the chemical potential for the monomer species in the solution by means of a technique that combines a slow-heating step with a controlled-rate delivery of additional precursors. In the reaction environment, the supersaturation threshold is crossed at a minimum temperature of 240–250 °C after a long induction period (Figure S6 in the Supporting Information). This suggests that active monomers necessary for building up the oxide network are secondary species<sup>44</sup> that accumulate slowly from aminolysis of the titanium carboxylate. The nucleation burst arrests as the supersaturation is relieved, following which a preferential enlargement of the embryos initially generated occurs at a comparatively faster rate over the production of additional nuclei (Scheme 1, path I–II). Such a self-regulated dynamics can be equally interpreted within the frame of the classical nucleation theory, according to which the activation energy for homogeneous nucleation in solution is much higher than the barrier for heterogeneous nucleation or

growth on pre-existing seeds.<sup>25</sup> The temporal separation between the nucleation and the growth stages, which is thereby realized in our syntheses, can be advantageously exploited to increase the nanocrystal dimensions as much as desired by continuously replenishing the titania precursors into the reaction media at a judiciously low rate. This mechanistic picture accounts for the rather narrow distribution of sizes and aspect ratios with which the nanorods can be ultimately synthesized by the employed experimental technique. In addition, the OLAM and OLAC surfactants at suitable ratios play two important roles: first, they dictate the relative balance of monomer consumption between the homogeneous and heterogeneous nucleation stages, thereby enabling tuning of the nanorod dimensions and the ultimate degree of shape anisotropy achievable; second, they assist anisotropic crystal development, as they can accentuate differences in growth rates along the various crystallographic directions by facet-selective adhesion mechanism.<sup>25–27</sup>

A less straightforward explanation is possible for which crystal phases are ultimately preferred at the nucleation and growth stages, respectively. Combined structural–morphological analyses have highlighted that the initial monomer supersaturation leads to homogeneous nucleation and fast growth of anatase (Scheme 1, path I–II), which is not only kinetically favored but also thermodynamically justified on the basis of the size dependence of structural stability of titania polymorphs at the nanoscale.<sup>2,28–33,45,46</sup> Whenever it forms, the anatase lattice eventually develops along its unique axis of symmetry.<sup>25,26</sup> Interestingly, the brookite polymorph is ascertained for nanorods that have surpassed certain dimensional limits, corresponding to sizes of approximately ~3–4 nm × 20 nm, as preliminarily

(44) (a) Casula, M. F.; Jun, Y.-w.; Zaziski, D. J.; Chan, E. M.; Corrias, A.; Alivisatos, A. P. *J. Am. Chem. Soc.* **2006**, *128*, 1675–1682. (b) Kwon, S. G.; Piao, Y.; Park, J.; Angappane, S.; Jo, Y.; Hwang, N.-M.; Park, J.-G.; Hyeon, T. *J. Am. Chem. Soc.* **2007**, *129*, 12571–12584.

(45) Zhang, H. Z.; Banfield, J. F. *J. Mater. Chem.* **1998**, *8*, 2073–2076. (46) Finnegan, M. P.; Zhang, H. Z.; Banfield, J. F. *J. Phys. Chem. C* **2007**, *111*, 1962–1968.

suggested by XRD and further highlighted by statistical HRTEM analyses (Figures S8–S13 in the Supporting Information).

According to XRD studies, the emergence of brookite is accompanied by disappearance of the pristine anatase domains, while TEM reveals that the nanocrystals evolve steadily to larger dimensions and higher aspect ratios. These pieces of evidence discredit the hypothesis of dissolution/recrystallization processes as a possible pathway for brookite formation.<sup>2</sup> Involvement of such mechanisms would imply a nanocrystal growth sequence, in which the initial anisotropic development in the anatase phase should temporarily be interrupted and reverse back toward a size shrinking regime, eventually terminating in particle disappearance. After the latter event, a renewed burst of homogeneous nucleation in the brookite structure should set in new rod-generating conditions. However, such an evolution has never been observed experimentally.

As an additionally interesting piece of information gathered from our statistical HRTEM analyses (Figures S11–13 in the Supporting Information), the majority of the smaller and more isotropic particles that may occasionally contaminate the brookite samples are made of anatase and possess structural features dissimilar from those of the anatase nanorod seeds (e.g., irregular shapes and sizes, unusual growth elongation direction, and types of crystallographic facets exposed). Besides supporting the arguments just discussed above, this fact implies that direct homogeneous nucleation of brookite, which would hence lead to tiny nanocrystals in this phase only, is likely disfavored at all synthesis stages. Hence, random reaction fluctuations may eventually result in secondary nucleation of undesired anatase nanocrystals that will, however, evolve independently.

Taken together, all above observations allow us to propose that brookite could originate via direct solid-state phase transformation of the initially formed *c*-axis-elongated anatase seeds (Scheme 1, path III), following which further growth continuation could occur exclusively in the orthorhombic phase (Scheme 1, path IV–VI). Figure 7 shows an example of TiO<sub>2</sub> nanorods that can be traced back to the phase transition stage (Scheme 1, path IV) and support our hypothesis. Indeed, the HRTEM image (Figure 7a) reveals a biphasic object, in which two different regions can be unambiguously indexed to brookite and anatase, respectively, as inferred by the relevant FFT analyses (Figure 7c–d). The two portions show a clear continuity between the  $\{-1,1,-1\}$  brookite planes ( $d_{-1,1,-1} = 0.346$  nm) and the  $\{0,1,-1\}$  anatase planes ( $d_{0,1,-1} = 0.352$  nm), as evidenced also by the merging of two diffractograms (Figure 7e). An interface can be recognized, that extends over less than  $\sim 1$  nm, as expected when brookite and anatase domains are joint. As a further analytic tool, we have derived a detailed map of the crystal-phase localization within the hybrid nanocrystal by assessing variations in the local amplitude of a periodicity characteristic of each polymorph, using a previously established method<sup>40</sup> (see the Experimental Section). The as-derived false-color crystal-phase map image clearly unravels the topological distribution of the anatase and brookite domains, evidencing a sharp separation between them. Finally, a further hint of incomplete restructuring can be deduced from the observation that the heteronanostructure is enclosed by a corrugated perimeter rather than by well-defined facets (Figure 7a).

At the in-depth level of examination reached here, further important remarks deserve emphasis. On one hand, it should be highlighted that the most developed longitudinal  $\{2,1,0\}$  facets of the fully grown rodlike brookite nanocrystals are

structurally similar to the  $\{011\}/\{101\}$  plane families which constitute the lateral sidewall zigzag patterns of *c*-axis-elongated anatase nanorods.<sup>2,16,26,36,37</sup> This can be in turn related the effectiveness of the employed surfactants in lowering the surface energies of those particular facets among the various surfaces exposed, thereby justifying the uninterrupted anisotropic growth regime via facet-preferential ligand adhesion during the crystal-phase conversion process.<sup>25,26</sup> Other common structural motives can be found, as, for example, between the  $\{1,0,0\}$  facets of the brookite nanorods and the  $\{1,1,2\}$  planes of anatase,<sup>43</sup> while comparative examination of the relevant lattice distances points out that the spacings of  $\{210\}$  and  $\{220\}$  brookite planes ( $d_{210} = 0.350$  nm,  $d_{220} = 0.2332$ ) are actually close to those of  $\{011\}$  and  $\{004\}/\{112\}$  anatase planes ( $d_{011} = 0.352$  nm,  $d_{004} = 0.2379$ ,  $d_{112} = 0.2332$ ), respectively. Overall, the high degree of similarity between the two TiO<sub>2</sub> crystal structures, the recognition of hybrid nanocrystals with epitaxially interconnected domains of the two polymorphs during the crystal-phase transition stage, as well as the characteristic lattice elongation in the *c*-axis direction for both the anatase seeds and the final brookite nanostructures indeed support the feasibility of a solid-state phase interconversion process that could proceed via highly correlated atomic displacement pathways<sup>40–50</sup> (Scheme 1, path IV). On the other hand, it is additionally worth noting that, within the limits of HRTEM statistics, those particular types of hybrid anatase–brookite nanorod architectures identified above are mainly confined to nanocrystal samples in the 20–30 nm length size regime that immediately follows the initial anatase-dominated synthesis period. Moreover, their relative abundance is always very low (less than 2% of the total population). These facts highlight that the anatase-to-brookite phase change is much faster than the average growth rate of the nanocrystals, which in fact explains why it has been experimentally difficult to capture the system at gradually distinct periods of advancement of the structural conversion process.

We rationalize the anatase-to-brookite transition as arising from the interplay of thermodynamic and kinetic effects. On one hand, it should be considered that, in a nanocluster, the contribution of the free surface energy to the total energy is much more influential than in a macroscopic solid, for which the chemical potential of the elemental components is practically the most relevant term. We propose that the rod-shaped anatase seeds can grow fast until they eventually approach a critical size and shape anisotropy threshold, at which the crossover for polymorph stability reversal is reached. Indeed, owing to the closeness of the bulk free energy values of anatase and brookite,<sup>29</sup> progression toward such transition point could be easily promoted by large alterations in the nanocrystal surface free energy, which would arise from the decreased chemical potential of the solution monomers (following precursor consumption during growth), and from the dynamic binding of solution species to the particle surface. A thermodynamic driving force can therefore exist at a critical nanocrystal volume,<sup>2,25–33,36e,45,46</sup> which could induce solid-state

(47) (a) Gribb, A. A.; Banfield, J. F. *Am. Mineral.* **1997**, *82*, 717–728. (b) Zhang, H. Z.; Banfield, J. F. *J. Phys. Chem. C* **2007**, *111*, 6621–6629.

(c) Fernandez-Garcia, M.; Wang, X.; Belver, C.; Hanson, J. C.; Rodriguez, J. A. *J. Phys. Chem. C* **2007**, *111*, 674–682.

(48) (a) Penn, R. L.; Banfield, J. F. *Science* **1998**, *281*, 969–971. (b) Gilbert, B.; Zhang, H.; Huang, F.; Finnegan, M. P.; Waychunasc, G. A.; Banfield, J. F. *Geochem. Trans.* **2003**, *4*, 20–27.

(49) Penn, R. L.; Banfield, J. F. *Am. Mineral.* **1999**, *84*, 871–876.

(50) Penn, R. L.; Banfield, J. F. *Am. Mineral.* **1998**, *83*, 1077–1082.

conversion of the initially formed anatase nanorods into brookite, thereby guaranteeing further growth in the latter crystal phase only (Scheme 1, path IV–VI). In addition, the general result of growing brookite nanorods through judiciously low supply of precursors indicates that low monomer supersaturation in the solution set near-equilibrium growth conditions that can facilitate formation of more thermodynamically stable polymorphs other than anatase.<sup>26,51</sup>

On the other hand, the aforementioned thermodynamic requirements alone do not suffice to explain the present experimental findings exhaustively. A major inadequacy in fact emerges from our control seeded-growth experiments,<sup>25</sup> in which presynthesized (and purified) surfactant-capped phase-controlled nanorods were introduced into typical brookite-generating mixtures (see Figure S14 in the Supporting Information). The temporal size-morphological evolution of the particle population reveals that such foreign seeds remain virtually unchanged in size and crystal structure, over a wide range of reaction conditions, whereas the nanocrystals generated *denovo* from the solution precursors evolve independently in the form of brookite nanorods, as in our standard syntheses. These findings strongly indicate that additional kinetically driven processes should play a complementary important role in the formation of brookite. In this regard, it should be considered that direct homogeneous nucleation of brookite as well as its solid-state transformation from anatase requires a high activation energy barrier to be overcome.<sup>28,29,45,47</sup> We thus suggest that an alternative and more convenient pathway that could trigger phase transformation would involve an initial heterogeneous nucleation of brookite onto the anatase seeds. For example, it has been previously demonstrated that during hydrothermal coarsening of nanosized titania, imperfect oriented attachment among particles of one polymorph can lead to the formation of defects (e.g., dislocations, twin planes, or other interfaces) containing structural motives common to other crystal phases.<sup>48–50</sup> These defects can then serve as low-energy sites for nucleating a different polymorph, thereby destabilizing the phase underneath and stimulating progression of polytypic transformation via lattice atom redistribution.<sup>49,50</sup> In our growing media, brookite can presumably originate on critical anatase seeds that have developed appropriate sets of facets, edges, or corners (Scheme 1, path III) at which the activation barrier for heterogeneous nucleation may be appreciably decreased. Starting from such interfaces, crystal-phase conversion should then proceed fast (Scheme 1, path IV) through well-concerted anatase–brookite atomic rearrangement pathways that would be inherently favored by the close structural similarities between the two lattices. Overall, the sharpness of the anatase–brookite phase transition and the scarce abundance of mixed-phase heterostructured nanocrystals assessed by us disclose for brookite a rate law based on a slow (heterogeneous) nucleation step and subsequent rapid growth stage.<sup>49,50</sup> The unsuccessful attempts to achieve anisotropic growth continuation on foreign nanorods, regardless of their crystal-phase, indicates that the seeds should fulfill a number of subtle requirements, in terms

of surface structural features and chemical reactivity, which can only be realized when they are generated *in situ* and their growth is dynamically self-regulated under a suitable chemical potential of the solution.

Finally, another interesting aspect deserving remark is that, as opposed to what has been commonly reported for nanosized TiO<sub>2</sub> prepared by both aqueous<sup>2,45–50</sup> and non-aqueous routes,<sup>2,26,27,36e</sup> the expected formation of rutile at relatively large nanorod sizes (>80–100 nm) has never been observed under our synthesis conditions. In this regard, an important action could be played by the surfactants as well as by the particular titanium complexes and monomer species present in the solution. The dynamic adhesion of such molecular species to the growing nanocrystals could contribute, through both electronic and sterical surface effects, to stabilize those specific sets of brookite facets exposed to such a great extent as to kinetically freeze<sup>26,51</sup> the nanorods in the orthorhombic structure over a significantly broad size range.

#### 4. Summary and Conclusions

In summary, we have described a surfactant-assisted nonhydrolytic strategy to synthesize anisotropic TiO<sub>2</sub> nanocrystals with tunable aspect ratios in the hardly accessible brookite crystal structure, demonstrating unprecedented ability to regulate the geometric parameters of the resulting nanostructures in a systematic way over a wide dimensional range. Our investigations have allowed us to infer a self-regulated phase-switching seed-catalyzed mechanism, in which initially generated anatase seeds trigger heterogeneous nucleation of brookite and promote subsequent growth of the nanorods in the latter phase controllably. In this picture, the time variation of the chemical potential for the monomer species in the solution, the size dependence of structural stability of the relevant titania polymorphs, and the reduced activation barrier for heterogeneous brookite nucleation onto the seeds have been considered to play crucial roles. To our best knowledge, it is the first time that such formation pathways have been directly assessed for nonaqueous colloidal TiO<sub>2</sub> systems. The availability of high-quality anisotropic brookite TiO<sub>2</sub> nanocrystals can be expected to deliver novel interesting technological opportunities in the exploitation of crystal-phase-controlled nanomaterials. The achievements of this study can be of both fundamental and practical importance in the development of advanced synthetic tools to structurally refined nanotitania with higher degree of functionality.

**Acknowledgment.** This work was partially supported by the Italian Ministry of Research (contract no. RBIN048TSE) and by the European project SA-NANO (contract no. STREP 013698). The authors thank G. Caputo for assistance in FT-IR measurements and Dr. L. Manna for many inspiring discussions.

**Supporting Information Available:** Fittings of XRD patterns, HRTEM simulations, FT-IR studies on the mechanism of aminolysis reaction, HRTEM statistical analyses, control seeded-growth experiments. This material is available free of charge via the Internet at <http://pubs.acs.org>.

JA803559B

(51) (a) Kim, Y.-H.; Jun, Y.-w.; Jun, B.-H.; Lee, S.-M.; Cheon, J. *J. Am. Chem. Soc.* **2002**, *124*, 13656–13657. (b) Cozzoli, P. D.; Manna, L.; Curri, M. L.; Kudera, S.; Giannini, C.; Striccoli, M.; Agostiano, A. *Chem. Mater.* **2005**, *17*, 1296–1306.